

Spontaneous Conducting Boundary Channels in 1T-TaS₂

T. R. Devidas¹, Jonathan T. Reichanadter^{2,3}, Shannon C. Haley^{2,3}, Matan Sterenberg⁴, Joel E. Moore^{2,3}, Jeffrey B. Neaton^{2,3}, James G. Analytis^{2,3,5*}, Beena Kalisky^{1*}, Eran Maniv^{4*}

¹Department of Physics and Institute of Nanotechnology and Advanced Materials, Bar-Ilan University, Ramat Gan 5290002, Israel

²Department of Physics, University of California, Berkeley, California 94720, USA

³Materials Science Division, Lawrence Berkeley National Laboratory, Berkeley, California 94720, USA

⁴Department of Physics, Ben-Gurion University of the Negev, Beer-Sheva 84105, Israel

⁵CIFAR Quantum Materials, CIFAR, Toronto, Canada

* Corresponding authors: Email: analytis@berkeley.edu, beena@biu.ac.il, eranmaniv@bgu.ac.il

Materials that transition between metal and insulator, the two opposing states that distinguish all solids, are fascinating because they underlie many mysteries in the physics of the solid state. In 1T-TaS₂, the metal-insulator transition is linked to a series of metastable states of a chiral charge density wave whose basic nature is still an open question. In this work, we show that pulses of current through these materials create current-carrying boundary channels that distinguish the metallic and insulating states. We demonstrate electrical control of these channels' properties, suggesting their formation could be due to the complex interplay of the formation of domain walls and the viscous flow of electrons. Our findings show that physical boundaries play a key role in the properties of the metastable states of the metal-insulator transition, highlighting new possibilities for in-situ electrical design and active manipulation of electrical components.

Electrons flowing in a metal often behave as a liquid flowing through a channel. When a liquid flows through anisotropic media that breaks rotational, inversion and/or time-reversal symmetry, many fascinating effects can arise, such as odd-parity Hall viscosity and exotic boundary states (1, 2). Electronic flow effects are seldom studied in conjunction with the physics of metal-insulator transitions, and even less so in materials where the flow influences the transition itself. Yet such systems open new possibilities for non-equilibrium electrical responses with applications in quantum sensing (3), ultrafast switching (4, 5), and neuromorphic computing (6).

The transition-metal dichalcogenide (TMD) 1T-TaS₂ is the subject of extensive research in electron transport and an ideal system for investigating correlated electron flow in an anisotropic medium. This layered metal orders at 550K into an Incommensurate Charge Density Wave (I-CDW) phase, followed by a nearly commensurate CDW (N-CDW) ordering at ~350 K(7, 8). It then undergoes a metal-insulator transition below ~180 K that induces the formation of a commensurate CDW (C-CDW) lattice composed of $\sqrt{13}\times\sqrt{13}$ Star-of-David (SD) hexagram atomic distortions. This state has been proposed to result from a Mott transition, where Coulomb interactions drive electron localization(9–11). Interestingly, the C-CDW state of 1T-TaS₂ has been shown to exhibit tunable metallicity as a result of voltage or laser pulsing(4, 12). Scanning tunneling microscopy (STM) studies of electrically pulsed 1T-TaS₂ nano-flakes have shown that such conducting and non-conducting states arise from a continuum of metastable states (13) related

to the density and topology of domain boundaries in the underlying CDW (14–16). Recent studies using angle-resolved photoemission spectroscopy (ARPES) (17) and Raman response (18) have revealed that C-CDW domains are intrinsically chiral whose domain walls can be manipulated by voltage pulses.

However, as noted in the latter study (18), the interplay of chirality and electrical control remains somewhat mysterious, without an obvious mechanism connecting the material’s symmetry to experimental observations. The point group of the C-CDW structure is C_{3i} , a reduced symmetry group when compared with D_{3d} of the pristine crystal(19). This transition preserves inversion yet omits certain mirror symmetries, and while the broken mirror symmetry distinguishes left and right chiral domains, it does not allow linear coupling to an in-plane electric field. The only coupling that is allowed is either quadratic, or through the domain walls themselves, due to their lower symmetry.

The anisotropy of a material’s conductivity is a key property linking internal symmetries of a system to its electrical response. Studies examining the conductive properties of 1T-TaS₂ in the C-CDW low-temperature regime (8, 20, 21) have generally overlooked this property, leaving a critical gap in our knowledge of these materials. In this work, we explore the electrical control of the *anisotropic* conductivity of this system, revealing a robust, non-volatile switching between “resistive states” defined by the direction of externally applied electrical pulses. We find that the origin of this anisotropy is not solely a result of defects in the bulk order, but relies on the spontaneous creation of a current-carrying boundary channel along a single physical edge of the material. We identify an electrical protocol to control which boundary the channel forms along and how to electrically write and erase the boundary channel so that the system transitions between an anisotropic good conductor and a homogeneously poor conductor. Our data suggest that the orientation of the electrical pulse dynamically affects the creation and annihilation of current-carrying paths, in a manner that has possible analogies to phenomena seen in viscous flow in anisotropic media (1, 22). We directly imaged the actual flow of electric current and found surprising behaviors that hold information about the underlying CDW phases. The most crucial piece of information is that the low-resistive state manifests itself as single-sided boundary channels, a behavior that was not known or predicted, and will surely contribute towards resolving earlier findings (12, 23–27), yet also reveal new questions, like the origin of the boundary states themselves, and the dynamic interplay between the current and the internal broken symmetries of the system.

Building upon the voltage switching studies of preceding works (20, 28, 29), we fabricate crossbar devices to investigate transport anisotropies in the system. The three-fold rotational symmetry of the CDW order, shown in Fig. 1A would naively exclude any such anisotropy. However, domain walls have much lower symmetry and in principle, should couple to currents or electric fields, resulting in an anisotropic response (29). Given their known role in the conductivity of the system, and their coupling to in-plane electric fields (14, 20), these effects are important to investigate.

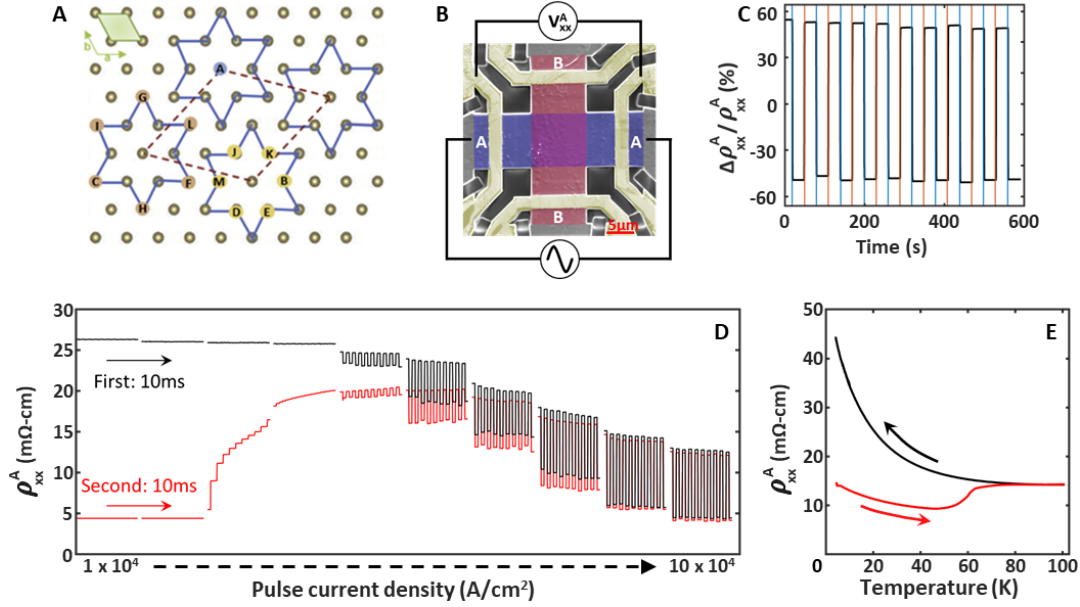


Fig. 1. Directional switching in 1T-TaS₂. (A) Unit cell (top left) and star-of-David (SD) charge density wave (CDW) structure in 1T-TaS₂ (30). Only Tantalum atoms are visualized for convenience. (B) Scanning electron microscope image of a 1.4 μm thick 1T-TaS₂ device (device I). False color overlays, blue and red, show the two d.c. pulse bars A and B, respectively. The a.c. probe current is directed along the A pulse bar. (C) Two-level resistivity switching established by application of 10 d.c. pulses (10^5 A/cm², 10ms) alternated between the A and B pulse bars at 2K. Pulsing along the probe channel A lowers the resistivity and pulsing along the orthogonal channel B increases the resistivity. Y axis presents the percentage switching change and is calculated by $100 \cdot (\rho - \langle \rho \rangle) / \langle \rho \rangle$, where $\langle \rho \rangle$ is the integrated average resistivity. (D) Pulse amplitude dependence of resistivity switching response at 2K. D.C. pulses of increasing amplitudes (1×10^4 - 10×10^4 A/cm²) at a constant pulse width of 10ms are applied sequentially to the device in A-B configuration. The set of measurements labeled “First: 10ms” are recorded from the high resistivity “insulating” state achieved after cooling the device through the N-CDW to C-CDW transition. The set of measurements labeled “Second: 10ms” are recorded after the first cycle. (E) Temperature dependent resistivity of device III measured before (black) and after (red) switching to low resistivity by application of d.c. pulses. The black/red arrows indicate the temperature evolution during the black/red measurement cycle.

Crossbar devices are fabricated using a focused ion beam (FIB), as discussed in the methods section, and are generally much thicker in comparison to previous studies of electrical switching, ranging between 0.5-5 microns. A device shown in Fig. 1B, is pulsed along two perpendicular directions (A and B) with a direct “write” current (10^4 - 10^5 A/cm²), and the longitudinal resistivity ρ_{xx}^A is subsequently measured using a significantly lower a.c. probe, or “read” current. This yields a robust, non-volatile pulse train of switching between a high-resistance state and a low-resistance state, differing by nearly a factor of 2 (Fig. 1C). 1T-TaS₂ shows a dramatic anisotropic resistivity upon current pulsing. The pulse trains are riding on an overall background resistance (Fig. 1D). The sample is cooled to a high resistance state (typically described as “insulating”, ~ 25 m Ω -cm) and then a train of current pulses along A and B are applied with progressively larger currents. During this process, the resistance monotonically decreases: we observe no change until $\sim 5 \times 10^4$ A/cm² where the resistance begins to switch, and the overall background resistance starts to decrease. When the current is pulsed along A, a low resistance is recorded along V_{xx}^A , and when pulsed along B, a high resistance is recorded along V_{xx}^A . Once the maximum switching current is applied ($\sim 10^5$ A/cm²), the system is stable in a lower resistance state (~ 5 m Ω -cm). When the pulse train sequence is applied again, no switching is observed for currents $< 5 \times 10^4$ A/cm². However, the background resistivity can be seen to increase with *every* pulse, before switching again. For

intermediate currents, the system gradually reverts toward its high resistance state, a phenomenon similar to previous observations in voltage pulse experiments (31). Moreover, thermal cycling after the device has been switched to its low resistance state (Fig. 1E), shows similar behavior of the metal-to-insulator transition observed by laser and electrical switching studies (20, 32).

To resolve the mechanism underlying this anisotropic conductivity response, we employ scanning SQUID magnetometry to image the current paths through the device between switching events. The scanning magnetic probe maps current flow from the generated magnetic fields in a non-invasive, *operando* characterization.

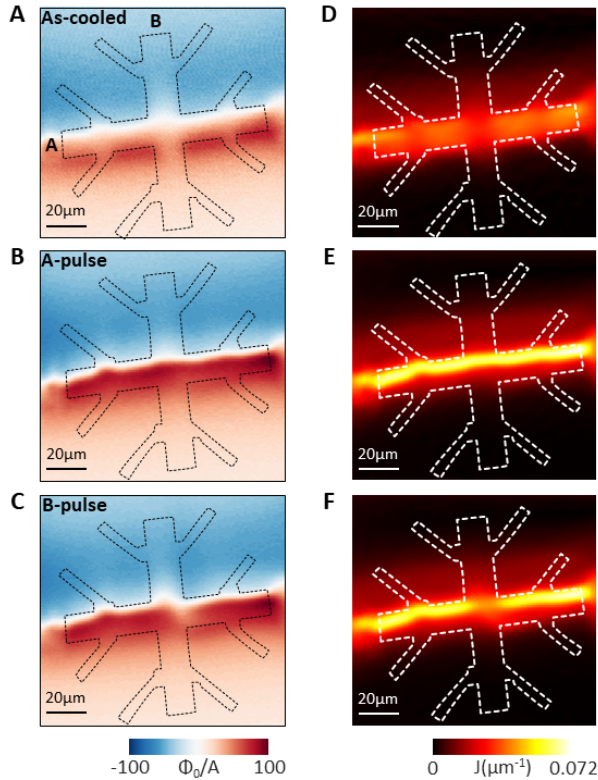


Fig. 2. Mapping magnetic flux response to current flow reveals a conducting boundary channel. (A) Scanning SQUID image (raw) of the magnetic flux generated by probe-current ($10 \mu\text{A}$) flowing along the A-pulse bar of a fabricated 1T-TaS_2 device (device II) in as-cooled configuration at 4.2 K. The device is then subjected to d.c. pulses ($12.5 \times 10^4 \text{ A/cm}^2$, 10ms, Fig. S1A) along the A and B pulse bars, alternatingly. A repeated scan after (B) A-pulse and (C) B-pulse. Reconstructed current density map of the device in (D) As-cooled, (E) after A-pulse and (F) after B-pulse configurations. The current flows over the entire device in the as-cooled state. After the application of d.c.pulses, the current flow is confined to a boundary channel along the length of the channel after A-pulse and disrupted along the pulse bar junction after B-pulse.

The spatial current maps reveal significantly distinct electric current paths through the device between switching events. Current flow in the pre-pulse state is generally homogeneous, spreading over the entire bar (Fig. 2A, D). After a single write pulse into the low-resistance state, a pronounced conducting boundary channel (CBC) forms; the current flows along a narrow boundary channel that bridges the crossbar (Fig. 2B, E). The actual width of the boundary channel is below our spatial resolution (Supplementary data, Fig. S2.). The connection between lower resistivity and a reduced spatial channel contradicts classical intuition, suggesting that CBC conduction relies on a more exotic physical mechanism than one offered by geometric considerations. When we pulse along the perpendicular direction, the CBC is interrupted and the bridge is destroyed, leading to a high resistance state. The CBC is untouched on either side of the crossbar, showing that both the creation and annihilation of the channel are directly tied to the direction of the current pulse.

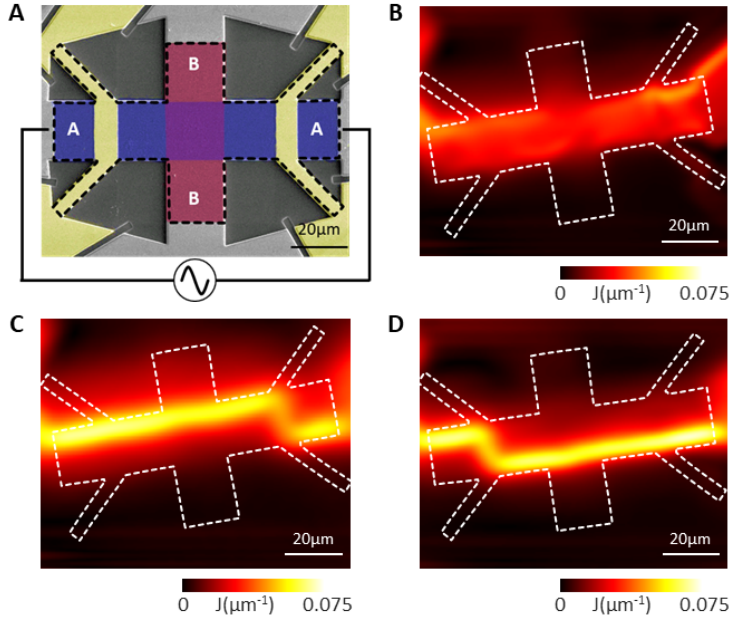


Fig 3. Edge switching of CBC. (A) SEM image of a 1T-TaS₂ device (device III). The a.c. probe current is marked on the device and directed along the A pulse bar. The d.c. pulse bars are indicated by the false color overlays red (A) and blue (B), respectively. (B) Reconstructed current density map of the device in as-cooled state. The device is subjected to a train of d.c. pulses (5.93×10^4 A/cm², 10ms) alternatively along A and B pulse bars. An additional A-pulse is added and the device is imaged. (C) and (D) are reconstructed current density maps in the device after the application of the additional A-pulse. The images were separated by thermal cycling of the sample to room temperature.

The boundary channel is a highly conducting path that leads to the low resistance state, explaining the switching effects observed in Fig. 1C. However, this raises questions regarding the boundary channels, namely which structural, chemical, and charge density lattice properties dictate the creation and location of the CBC. In Fig. 3, we illustrate a device where the boundary channel appeared on the top side during one cooldown, and on the opposite side in a separate cooldown. The choice of “which edge” pins the CBC appears to be spontaneous, suggesting that it may depend on the spontaneous symmetry breaking of the CDW domain structure.

We now study intermediate currents where the system returns to its “high resistance” state no matter the direction of the write-current (Fig. 1D). In Fig. 4 we execute a pulse protocol similar to that of Fig. 1D, but with only one pulse direction. Before pulsing, the current is homogeneously distributed in the bulk of the device and in the high resistance state (Fig. 4B). Applying a current pulse of density 12.5×10^4 A/cm² pushes the device into a low resistance state and the boundary channel forms, as expected (Fig. 4C). However, pulsing the device with intermediate value, drives the system back to its high resistance state. The spatial distribution of the current is almost exactly as it was on the first cooldown, flowing largely homogeneously through the sample (Fig. 4D). The intermediate pulses have annihilated the CBC.

The CDW domain walls (DW) in 1T-TaS₂ are widely thought to provide additional carriers to allow conduction (4, 33, 34), so these are natural candidates for the microscopic nature of the CBCs observed here, although domains of higher conduction cannot be ruled out (15, 28). Physical edges of samples form natural termination points for domain walls; simple free energy considerations would favor the formation of these channels at the boundary of the device. Furthermore, prior studies have demonstrated direct evidence for the electrical manipulation of the DWs (13, 28, 29). Notably, the CBCs follow areas of the device that create some kind of interface, like areas where the gold contacts have been deposited for resistivity measurements (Fig. 3(A,C-D)). The physical edge of the device is simply a special case of such an interface.

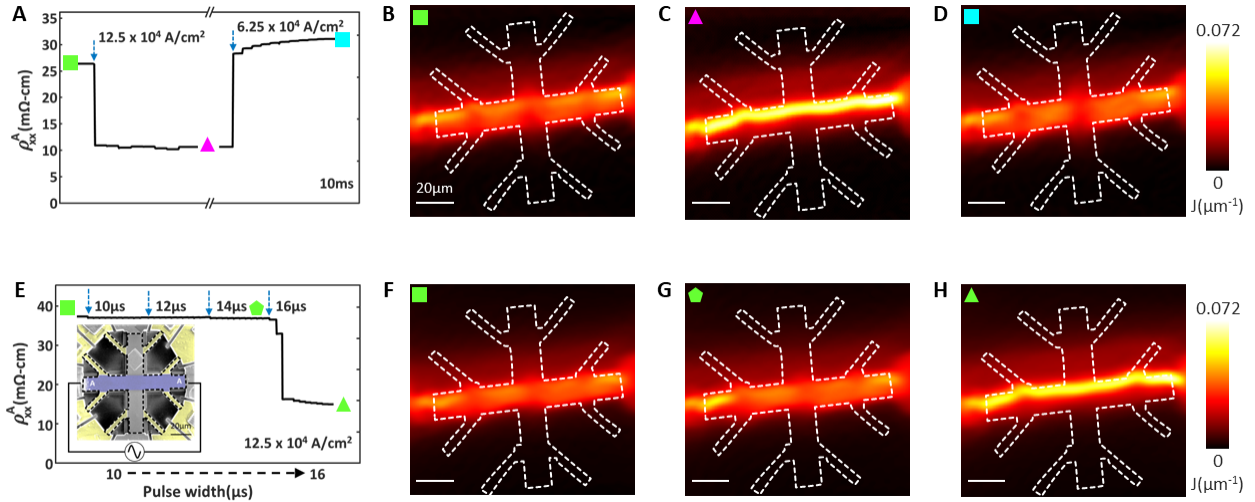


Fig 4. Creation/annihilation and pulse width dependence of CBC. (A) A typical resistivity response for application of d.c. pulses along the A pulse bar of device II (inset of panel (E)). The blue dashed lines indicate the start of application of a train of d.c. pulses along the A pulse bar. Green square, magenta triangle and blue square indicate the positions where scanning SQUID images are obtained. The reconstructed current density maps show that the device initially goes from (B) high resistance/largely homogeneous current flow to (C) low resistance/ boundary channel flow when subjected to d.c. pulses of density 12.5×10^4 A/cm 2 . The (D) high resistance/largely homogeneous flow is once again obtained by pulsing the device with d.c. pulses of density 6.25×10^4 A/cm 2 . The pulse width during this cycle is maintained at 10ms. (E) Resistivity response curve as a function of varying pulse width at a constant current density of 12.5×10^4 A/cm 2 . The blue dashed lines indicate a change in pulse width. Inset: SEM image of the 1T-TaS $_2$ device (device II). The reconstructed current density maps marked by (F) green square, (G) green pentagon and (H) green triangle, show that the formation of the CBC is instantaneous within a resolution of 2 μ s.

The preferred edge is independent of the pulse current polarity, (Supplementary data, Fig. S3(A-D)) and this supports our belief that the formation of the CBCs is a stochastic process. A possible driver could be thermal effects induced by Joule heating during the electrical pulses (35, 36). To investigate this, we study the progression of the formation of the boundary channel as a function of pulse width. The boundary channel begins forming at relatively short pulse widths, which occurs progressively over ten microseconds (Fig. 4E-H). However, the bridge across the crossbar region happens suddenly, in just fractions of a microsecond (certainly less than our ability to resolve); a clear indication of precipitous path formation. This seems an unnatural process if the effects were entirely thermal, which might be expected to evolve more smoothly.

A possible mechanism could be the interplay between the electron flow and the DW motion itself. In a recent study by Mraz et al. it was shown that pairs of topological defects defining DWs could be manipulated by in-plane electric fields, leading to transitions between conducting or insulating behavior; the flow of electrons can move and shrink entire domains (31). Consider, therefore, a process somewhat similar to electromigration or chiral separation (37–39), where the flow of electrons imparts momentum to atoms, causing them to migrate through a material due to a combination of diffusion and thermal effects. In the present case, the electrons may be imparting momentum to CDW clusters that nucleate along a physical edge, moving them until they form a bridge across the crossbar spanning tens of micrometers in length. An alternative process could be analogous to ‘viscous fingering,’ which is a poorly understood interfacial instability between fluids of different viscosity (40); in the present case ‘less viscous’ regions of conducting domain walls

may be displacing the ‘more viscous’ single domains, resulting in confined conduction paths of lower resistance.

It is unclear why there is only one physical edge that is preferred for the formation of the CBC, but we do know that it is independent of current polarity and that the choice of physical edge is spontaneous. The dominant chirality of the CDW order may be important; while the current polarity appears to have no role in choosing which edge the CBC will favor, the dominant chirality (which is spontaneously chosen) may ultimately determine the location of the boundary channels. Notably, in the study by Liu et al. (14), it was shown that DWs separating domains of opposite chirality had DW that moved perpendicular to the electric field direction. In the present study, the CBC is always parallel to the pulse direction, so that if it contains DWs, they must be parallel to the applied current.

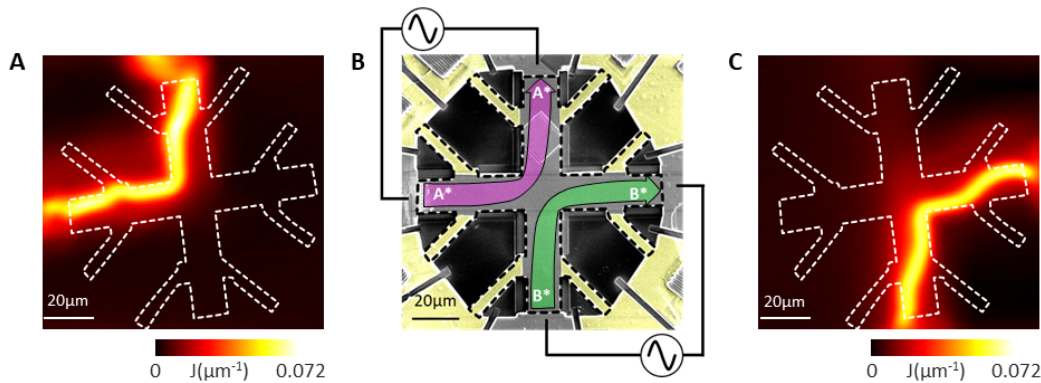


Fig. 5. Controllable confined path switching. (A,C) Conducting boundary channels after a train of d.c. pulses ($12.5 \times 10^4 \text{ A/cm}^2$, 10ms, fig. S1B) in the configuration shown in (B). (B) SEM image of a 1T-TaS₂ device (device II). The purple and green arrows indicate the direction of d.c. pulses applied alternately.

Other analogies in the fluid dynamics of chiral systems may be relevant; it was recently shown that robust boundary states appear in the rotational flow of a dissipative medium, which survive in the presence of barriers and turbulence, leading to the suggestion that they may have a topological origin (41). However, fluid flow in chiral media remains an active field of study, and electrons flowing in a chiral medium is perhaps an even richer physical system with exotic viscous effects associated with the motions of electrons or the CDW itself.

The dependence of the boundary channels on the direction (but not polarity) of the writing current and the geometric structure of its path opens the possibility of electrically controlling the position of the boundary channel itself. Application of current pulses along L-shaped paths (A* and B*) consistently formed CBC along the “inside lane” of the current path (Fig. 5). The CBC finds the shortest boundary path to ground, consistent with the suggestion that the nucleation of the boundary channel is a precipitous process that creates highly conducting interface channels.

The appearance of electrically induced conducting boundary channels in 1T-TaS₂ creates a mechanism for extreme transport anisotropy in this material and, to our knowledge, this is the first report of such states. While the mechanism for their formation is unknown, the boundary channels always choose only one physical edge, which is spontaneously chosen and, therefore, possibly linked to the chirality of the dominant domain of the CDW order. This will make the choice of physical edge sensitive to the geometric properties of the device, internal strains and even thermal

anisotropies in the material during cooling, opening the potential of using it as a sensor for new materials. Nevertheless, using specific current pulse protocols we are able to control the position of the boundary channel, suggesting ample possibilities for in-situ electrical design and active manipulation of electrical components in a single material platform. With the right device engineering, this could open new possibilities for technological applications of exotic materials.

References

1. G. Varnavides, A. S. Jermyn, P. Anikeeva, C. Felser, P. Narang, Electron hydrodynamics in anisotropic materials. *Nat. Commun.* **11**, 1–6 (2020).
2. J. E. Avron, R. Seiler, P. G. Zograf, Viscosity of Quantum Hall Fluids. *Phys. Rev. Lett.* **75**, 697 (1995).
3. C. L. Degen, F. Reinhard, P. Cappellaro, Quantum sensing. *Rev. Mod. Phys.* **89**, 035002 (2017).
4. L. Stojchevska, I. Vaskivskiy, T. Mertelj, P. Kusar, D. Svetin, S. Brazovskii, D. Mihailovic, Ultrafast switching to a stable hidden quantum state in an electronic crystal. *Science* **344**, 177–180 (2014).
5. J. del Valle, P. Salev, F. Tesler, N. M. Vargas, Y. Kalcheim, P. Wang, J. Trastoy, M.-H. Lee, G. Kassabian, J. G. Ramírez, M. J. Rozenberg, I. K. Schuller, Subthreshold firing in Mott nanodevices. *Nature* **569**, 388–392 (2019).
6. S. Prosandeev, J. Grollier, D. Talbayev, B. Dkhil, L. Bellaiche, Ultrafast Neuromorphic Dynamics Using Hidden Phases in the Prototype of Relaxor Ferroelectrics. *Phys. Rev. Lett.* **126**, 027602 (2021).
7. C. B. Scruby, P. M. Williams, G. S. Parry, The role of charge density waves in structural transformations of 1T TaS₂. *Philos. Mag.*, doi: 10.1080/14786437508228930 (1975).
8. P. Fazekas, E. Tosatti, Electrical, structural and magnetic properties of pure and doped 1T-TaS₂. *Philos. Mag. B*, doi: 10.1080/13642817908245359 (1979).
9. K. Rossnagel, On the origin of charge-density waves in select layered transition-metal dichalcogenides. *J. Phys. Condens. Matter* **23**, 213001 (2011).
10. D. Shin, N. Tancogne-Dejean, J. Zhang, M. S. Okyay, A. Rubio, N. Park, Identification of the Mott Insulating Charge Density Wave State in 1T-TaS₂. *Phys. Rev. Lett.* **126**, 196406 (2021).
11. A. W. Tsen, R. Hovden, D. Wang, Y. D. Kim, J. Okamoto, K. A. Spoth, Y. Liu, W. Lu, Y. Sun, J. C. Hone, L. F. Kourkoutis, P. Kim, A. N. Pasupathy, Structure and control of charge density waves in two-dimensional 1T-TaS₂. *Proceedings of the National Academy of Sciences* **112**, 15054–15059 (2015).
12. I. Vaskivskiy, I. A. Mihailovic, S. Brazovskii, J. Gospodaric, T. Mertelj, D. Svetin, P. Sutar,

- D. Mihailovic, Fast electronic resistance switching involving hidden charge density wave states. *Nat. Commun.* **7**, 11442 (2016).
13. J. W. Park, J. Lee, H. W. Yeom, Zoology of domain walls in quasi-2D correlated charge density wave of 1T-TaS₂. *npj Quantum Materials* **6**, 1–6 (2021).
 14. G. Liu, T. Qiu, K. He, Y. Liu, D. Lin, Z. Ma, Z. Huang, W. Tang, J. Xu, K. Watanabe, T. Taniguchi, L. Gao, J. Wen, J.-M. Liu, B. Yan, X. Xi, Electrical switching of ferro-rotational order in nanometre-thick 1T-TaS₂ crystals. *Nat. Nanotechnol.* **18**, 854–860 (2023).
 15. D. Cho, G. Gye, J. Lee, S.-H. Lee, L. Wang, S.-W. Cheong, H. W. Yeom, Correlated electronic states at domain walls of a Mott-charge-density-wave insulator 1T-TaS₂. *Nat. Commun.* **8**, 1–6 (2017).
 16. J. Skolimowski, Y. Gerasimenko, R. Žitko, Mottness collapse without metallization in the domain wall of the triangular-lattice Mott insulator 1T-TaS₂. *Phys. Rev. Lett.* **122**, 036802 (2019).
 17. H. F. Yang, K. Y. He, J. Koo, S. W. Shen, S. H. Zhang, G. Liu, Y. Z. Liu, C. Chen, A. J. Liang, K. Huang, M. X. Wang, J. J. Gao, X. Luo, L. X. Yang, J. P. Liu, Y. P. Sun, S. C. Yan, B. H. Yan, Y. L. Chen, X. Xi, Z. K. Liu, Visualization of Chiral Electronic Structure and Anomalous Optical Response in a Material with Chiral Charge Density Waves. *Phys. Rev. Lett.* **129**, 156401 (2022).
 18. Y. Zhao, Z. Nie, H. Hong, X. Qiu, S. Han, Y. Yu, M. Liu, X. Qiu, K. Liu, S. Meng, L. Tong, J. Zhang, Spectroscopic visualization and phase manipulation of chiral charge density waves in 1T-TaS. *Nat. Commun.* **14**, 2223 (2023).
 19. O. R. Albertini, R. Zhao, R. L. McCann, S. Feng, M. Terrones, J. K. Freericks, J. A. Robinson, A. Y. Liu, Zone-center phonons of bulk, few-layer, and monolayer 1T-TaS₂: Detection of commensurate charge density wave phase through Raman scattering. *Phys. Rev. B Condens. Matter* **93** (2016).
 20. D. Svetin, I. Vaskivskiy, S. Brazovskii, D. Mihailovic, Three-dimensional resistivity and switching between correlated electronic states in 1T-TaS₂. *Sci. Rep.* **7**, 46048 (2017).
 21. E. Martino, A. Pisoni, L. Ćirić, A. Arakcheeva, H. Berger, A. Akrap, C. Putzke, P. J. W. Moll, I. Batistić, E. Tutiš, L. Forró, K. Semeniuk, Preferential out-of-plane conduction and quasi-one-dimensional electronic states in layered 1T-TaS₂. *npj 2D Materials and Applications* **4**, 1–9 (2020).
 22. J. Perry-Houts, L. Karlstrom, Anisotropic viscosity and time-evolving lithospheric instabilities due to aligned igneous intrusions. *Geophys. J. Int.* **216**, 794–802 (2018).
 23. M. J. Hollander, Y. Liu, W.-J. Lu, L.-J. Li, Y.-P. Sun, J. A. Robinson, S. Datta, Electrically driven reversible insulator-metal phase transition in 1T-TaS₂. *Nano Lett.* **15**, 1861–1866 (2015).
 24. M. Yoshida, R. Suzuki, Y. Zhang, M. Nakano, Y. Iwasa, Memristive phase switching in

- two-dimensional 1T-TaS₂ crystals. *Sci Adv* **1**, e1500606 (2015).
25. D. Mihailovic, D. Svetin, I. Vaskivskiy, R. Venturini, B. Lipovšek, A. Mraz, Ultrafast non-thermal and thermal switching in charge configuration memory devices based on 1T-TaS₂. *Appl. Phys. Lett.* **119**, 013106 (2021).
 26. R. Venturini, A. Mraz, I. Vaskivskiy, Y. Vaskivskiy, D. Svetin, T. Mertelj, L. Pavlovič, J. Cheng, G. Chen, P. Amarasinghe, S. B. Qadri, S. B. Trivedi, R. Sobolewski, D. Mihailovic, Ultraefficient resistance switching between charge ordered phases in 1T-TaS₂ with a single picosecond electrical pulse. *Appl. Phys. Lett.* **120**, 253510 (2022).
 27. T. Patel, J. Okamoto, T. Dekker, B. Yang, J. Gao, X. Luo, W. Lu, Y. Sun, A. W. Tsen, Photocurrent Imaging of Multi-Memristive Charge Density Wave Switching in Two-Dimensional 1T-TaS₂. *Nano Lett.* **20**, 7200–7206 (2020).
 28. L. Ma, C. Ye, Y. Yu, X. F. Lu, X. Niu, S. Kim, D. Feng, D. Tománek, Y.-W. Son, X. H. Chen, Y. Zhang, A metallic mosaic phase and the origin of Mott-insulating state in 1T-TaS₂. *Nat. Commun.* **7**, 10956 (2016).
 29. D. Cho, S. Cheon, K.-S. Kim, S.-H. Lee, Y.-H. Cho, S.-W. Cheong, H. W. Yeom, Nanoscale manipulation of the Mott insulating state coupled to charge order in 1T-TaS₂. *Nat. Commun.* **7**, 10453 (2016).
 30. K. Momma, F. Izumi, VESTA 3 for three-dimensional visualization of crystal, volumetric and morphology data. *J. Appl. Crystallogr.* **44**, 1272–1276 (2011).
 31. A. Mraz, M. Diego, A. Kranjec, J. Vodeb, P. Karpov, Y. Gerasimenko, J. Ravnik, Y. Vaskivskiy, R. Venturini, V. Kabanov, B. Lipovšek, M. Topič, I. Vaskivskiy, D. Mihailovic, Manipulation of fractionalized charge in the metastable topologically entangled state of a doped Wigner crystal. *Nat. Commun.* **14**, 8214 (2023).
 32. I. Vaskivskiy, J. Gospodaric, S. Brazovskii, D. Svetin, P. Sutar, E. Goreshnik, I. A. Mihailovic, T. Mertelj, D. Mihailovic, Controlling the metal-to-insulator relaxation of the metastable hidden quantum state in 1T-TaS₂. *Sci Adv* **1**, e1500168 (2015).
 33. B. Sipos, A. F. Kusmartseva, A. Akrap, H. Berger, L. Forró, E. Tutiš, From Mott state to superconductivity in 1T-TaS₂. *Nat. Mater.* **7**, 960–965 (2008).
 34. Y. Liu (刘育), D. F. Shao (邵定夫), L. J. Li, W. J. Lu, X. D. Zhu, P. Tong, R. C. Xiao, L. S. Ling, C. Y. Xi, L. Pi, H. F. Tian, H. X. Yang, J. Q. Li, W. H. Song, X. B. Zhu, Y. P. Sun, Nature of charge density waves and superconductivity in 1T-TaSe_{2-x}Te_x. *Phys. Rev. B Condens. Matter* **94**, 045131 (2016).
 35. A. K. Geremew, S. Rumyantsev, F. Kargar, B. Debnath, A. Nosek, M. A. Bloodgood, M. Bockrath, T. T. Salguero, R. K. Lake, A. A. Balandin, Bias-Voltage Driven Switching of the Charge-Density-Wave and Normal Metallic Phases in 1T-TaS₂ Thin-Film Devices. *ACS Nano* **13**, 7231–7240 (2019).
 36. J. L. Hart, S. Siddique, N. Schnitzer, S. D. Funni, L. F. Kourkoutis, J. J. Cha, In operando

- cryo-STEM of pulse-induced charge density wave switching in TaS₂. *Nat. Commun.* **14**, 1–7 (2023).
37. P. G. de Gennes, Mechanical selection of chiral crystals. *EPL* **46**, 827 (1999).
 38. M. Kostur, M. Schindler, P. Talkner, P. Hänggi, Chiral separation in microflows. *Phys. Rev. Lett.* **96**, 014502 (2006).
 39. Marcos, H. C. Fu, T. R. Powers, R. Stocker, Separation of microscale chiral objects by shear flow. *Phys. Rev. Lett.* **102**, 158103 (2009).
 40. T. Gao, M. Mirzadeh, P. Bai, K. M. Conforti, M. Z. Bazant, Active control of viscous fingering using electric fields. *Nat. Commun.* **10**, 1–8 (2019).
 41. B. Favier, E. Knobloch, Robust wall states in rapidly rotating Rayleigh–Bénard convection. *J. Fluid Mech.* **895**, R1 (2020).

ACKNOWLEDGEMENT

T.R.D. and B.K. thank Shalev Gur for assistance with the scanning SQUID measurements.

Funding: Work by T.R.D. and B.K. was performed with support from the European Research Council grant no. ERC-866236, the Israeli Science Foundation grant no. ISF-228/22, the DIP KA 3970/1-1 and COST action SUPERQUMAP CA 21144. Work by J.G.A., J.E.M and S.C.H. was performed with support through a MURI project supported by the Air Force Office of Scientific Research (AFSOR) under grant number FA9550-22-1-0270. Work by M.S. and E.M. was performed with support from the European Research Council grant no. ERC-101117478, the Israeli Science Foundation grant no. ISF-885/23 and the PAZY foundation grant no. 412/23.

Author contributions: B.K., J.G.A and E.M. designed the experiments, T.R.D. and B.K. performed the scanning SQUID measurements and analyzed the data. S.C.H. and E.M. synthesized the samples. S.C.H., M.S and E.M. fabricated and characterized the devices. All the authors discussed the results and contributed to writing the manuscript. **Competing Interests:** The authors declare no competing financial interests. **Data and materials availability:** All data needed to evaluate the conclusions in the paper are present in the paper and/or supplementary materials.

Supplementary materials for **Spontaneous Conducting Boundary Channels in 1T-TaS₂**

Materials and Methods:

Crystal synthesis:

Single crystals of 1T-TaS₂ were grown via vapor transport using iodine as the transport agent. Stoichiometric amounts of tantalum and sulfur were mixed with 2.2 mg/cm⁻³ of iodine and sealed in a quartz ampoule, which was loaded into a horizontal two-zone furnace. The source end was held at 1050 °C and the sink end at 950 °C for a period of 7 days. High-quality crystals in dimensions excess of 1-2 mm were obtained after quenching the growth in ice water. Crystal structure and elemental stoichiometry were confirmed with powder X-ray diffraction and energy dispersive X-ray spectroscopy.

Device fabrication:

Focused Ion Beam (FIB) fabrication was performed by exfoliating single crystals of thicknesses under 10 μm and lateral dimensions of a few hundred micrometers onto sapphire substrates. 200 nm of gold was subsequently deposited over the sample and substrate. Using a Helios G4 FIB, gold was milled from the active area of the device, leaving a layer covering the sapphire substrate and edges of the crystal for electrical contacts. Platinum patches were added (via FIB deposition) connecting the edges of the device and the gold on the substrate (Fig. S4). The FIB was then used to mill the negative regions of the device and form the desired pattern. Contact resistances were of the order of a few ohms.

Scanning SQUID measurements:

Scanning SQUID microscopy was used to spatially map the current flow in the 1T-TaS₂ FIBed devices. An a.c. excitation (10-50 μA, 0.9-2 kHz) was driven across the sample channels. The magnetic field generated by the electric field was measured by rastering the SQUID's pickup loop over the sample. A 2D reconstruction of the current density using Biot-Savart's law visualizes the current distribution in the sample.

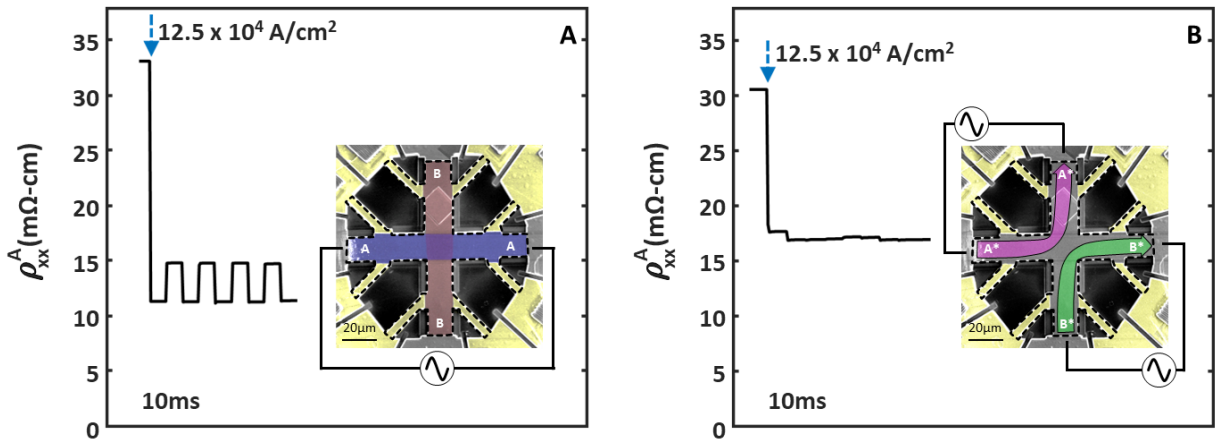


Fig. S1. Resistivity as a function of d.c. pulses (A) Resistivity response curve for device II for scanning SQUID data in Fig. 2. (main text). Inset - SEM image of the device with false color overlays on pulse bars A (blue) and B (red). The blue dashed arrow indicates the application of pulsed d.c. current of density $12.5 \times 10^4 \text{ A/cm}^2$. (B) Resistivity response curve for device II for scanning SQUID data in Fig. 5. (main text). Inset - SEM image of the device with false color overlays on pulse bars A* (purple) and B* (green). The blue dashed arrow indicates the application of pulsed d.c. current of density $12.5 \times 10^4 \text{ A/cm}^2$. The pulse width is 10 ms in both cases.

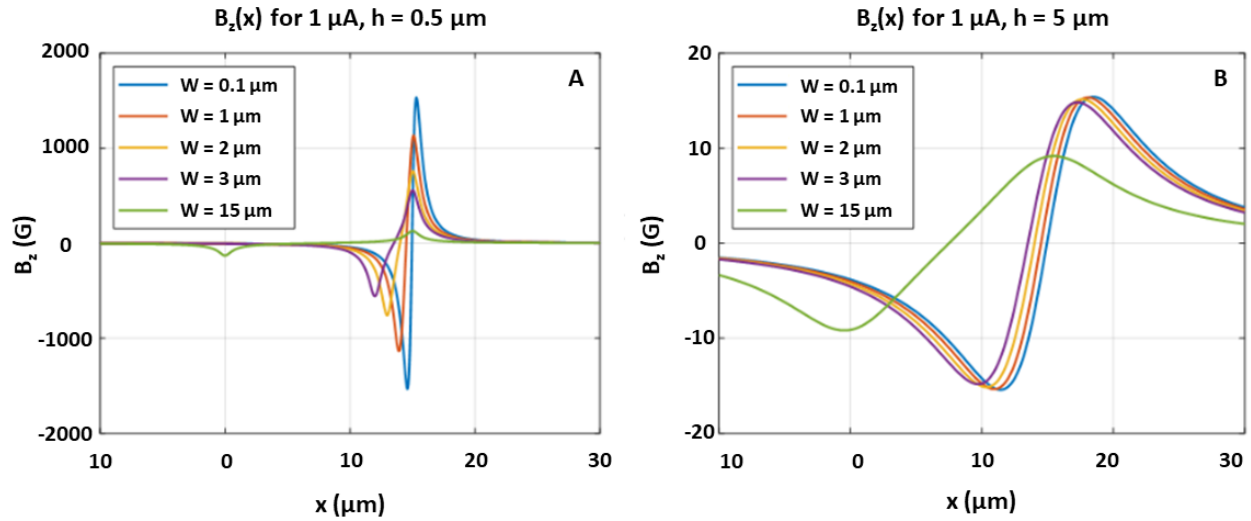


Fig. S2. Magnetic field distribution above current carrying sheets at different heights. The plots illustrate the variation in magnetic field intensity $B_z(x)$, in Gauss as a function of the horizontal distance across the current-carrying infinite sheets. The magnetic field is calculated using the Biot-Savart law. We simulate the magnetic fields in infinite sheets of widths ranging from $0.1 \mu\text{m}$ to $15 \mu\text{m}$, for $1 \mu\text{A}$ current. The magnetic fields are stronger and more focused for the narrower sheets. (A) $B_z(x)$ calculated for a sample-sensor separation of $0.5 \mu\text{m}$. (B) $B_z(x)$ calculated for a sample-sensor separation of $5 \mu\text{m}$.

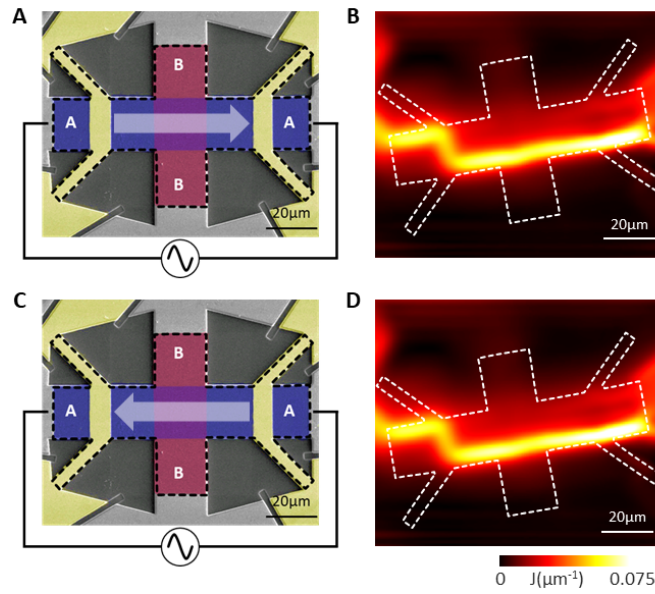


Fig. S3. Pulse polarity independence of CBC. (A,C) SEM image of 1T-TaS₂ device (device III) with false color overlays on pulse bars A (blue) and B (red). The device is subjected to a train of d.c. pulses ($5.93 \times 10^4 \text{ A/cm}^2$) along A and B pulse bars, alternately. The white arrow indicates the polarity/direction of the pulse applied along the A pulse bar. (B,D) Reconstructed current density maps from the scanning SQUID image of the device after application of A pulse.

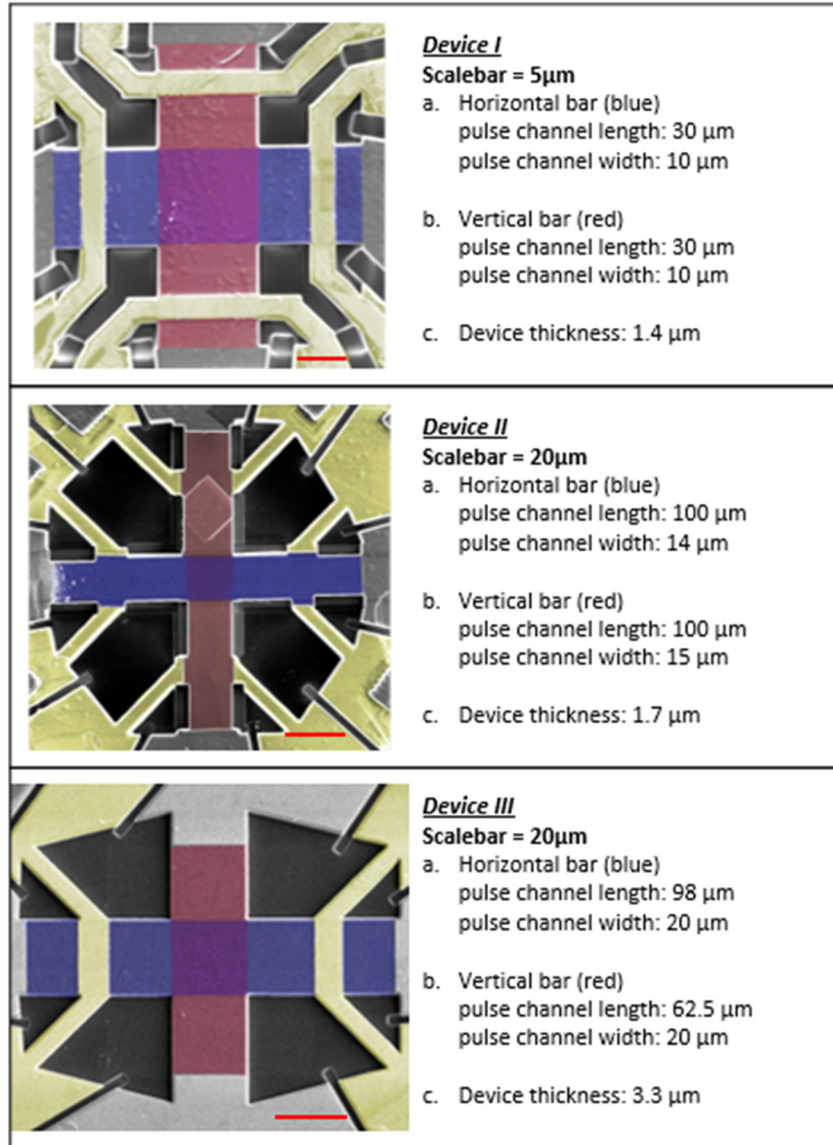


Fig. S4. Device Specifications. SEM images and dimensions of the three devices—device I, device II, and device III—investigated in this work.